

# High-Harmonic Generation from Monolayer and Bilayer Graphene

M. S. Mrudul<sup>1</sup> and Gopal Dixit<sup>1,\*</sup>

<sup>1</sup>*Department of Physics, Indian Institute of Technology Bombay, Powai, Mumbai 400076, India*  
(Dated: November 25, 2020)

High-harmonic generation (HHG) in solids is an emerging method to probe ultrafast electron dynamics in solids at attosecond timescale. In this work, we study HHG from a monolayer and bilayer graphene, exposed by an intense mid-infrared laser pulse. Bilayer graphene with AA and AB stacking are considered in this work. It is found that the monolayer and bilayer graphene exhibit significantly different harmonic spectra. The difference in the spectra is attributed to the interlayer coupling between the two layers. Pronounced interplay of intraband and interband contributions to the harmonic spectrum is found. Moreover, peculiar polarisation and ellipticity dependence are noticed in monolayer and bilayer graphene.

PACS numbers:

## I. INTRODUCTION

Thanks to technological advances that have enabled us to study strong-field driven processes in solids. Strong-field driven electron dynamics opens an avenue to control and understand carrier dynamics on the attosecond timescale<sup>1</sup>. High-harmonic generation (HHG) is one such strong-field driven process in which radiation with integer multiples of the incident driving frequency is emitted. After a pioneering work of Ghimire *et al.*<sup>2</sup>, HHG in solids has opened the door to study the electronic structure and its dynamics with the characteristic timescale in solids<sup>1,3</sup>. In recent years, HHG in solids has employed to explore several exciting processes such as band structure tomography<sup>4-6</sup>, probing the dynamics of the defects in solids<sup>7,8</sup>, the realisation of petahertz current in solids<sup>9,10</sup>, Bloch oscillations<sup>11,12</sup> are few to name. Moreover, HHG in solids offers an attractive all-solid-state compact optical device to obtain coherent and bright attosecond pulses in extreme ultraviolet energy regime<sup>1,3,13</sup>.

The realisation of atomically-thin monolayer graphene has catalysed a series of breakthroughs in fundamental and applied sciences<sup>14</sup>. Graphene shows unusual electronic and optical properties in comparison to its bulk counterpart<sup>15</sup>. The unique electronic structure of graphene exhibits varieties of nonlinear optical processes<sup>16-18</sup>. HHG from monolayer and few-layer graphene have been extensively studied in the past<sup>19-30</sup>. The underlying mechanism of HHG in graphene<sup>31</sup> was different from the one explained using a two-band model by Vampa *et al.*<sup>32</sup>. The intraband current from the linear band-dispersion of graphene was expected to be the dominating mechanism<sup>28,29</sup>. This is a consequence of the highly non-parabolic nature of the energy-bands<sup>2</sup>. In contrast to this prediction, the interband and intraband mechanisms in graphene are found to be coupled<sup>22,25,26</sup>, except for low intensity driving fields<sup>22</sup>. Vanishing band-gap and diverging dipole matrix element near Dirac points lead to strong interband mixing of valence and conduction bands in graphene<sup>31,33</sup>. The ellipticity dependence of HHG from graphene has been observed experimentally<sup>23,25</sup> as well as discussed

theoretically<sup>23-26</sup>. Atomic-like ellipticity dependence was reported by Taucer *et al.*<sup>25</sup>, whereas a higher harmonic yield for a particular ellipticity was observed by Yoshikawa *et al.*<sup>23</sup>. This anomalous ellipticity dependence was attributed to the strong-field interaction in the semi-metal regime<sup>23,34</sup>.

Along with monolayer graphene, bilayer graphene is also attractive due to its special optical response<sup>35</sup>. A bilayer graphene can be made by stacking another layer of the monolayer graphene on top. Three suitable configurations are possible for the bilayer graphene: (a) AA stacking in which the second layer is placed exactly on top of the first layer, (b) AB stacking in which B atom of the upper layer is placed on the top of A atom of the lower layer, whereas the other type of atom occupies the centre of the hexagon, and (c) twisted bilayer in which the upper layer is rotated by an angle with respect to the lower layer. AB stacking, also known as the Bernal stacking, is the one which is more energetically stable structure and mostly realised in experiments [see Fig. 1(b)]<sup>36,37</sup>. Recently, electron dynamics<sup>38,39</sup> and valley polarisation in bilayer graphene on ultrafast timescale is discussed theoretically<sup>40</sup>. The role of multiphoton resonant excitations in HHG for AB stacked bilayer graphene<sup>41</sup> as well as HHG from twisted bilayer graphene has been explored recently<sup>42</sup>. However, the comparison of HHG from monolayer and bilayer graphene; and a thorough investigation of the role of interlayer coupling are unexplored.

In this work, we explore HHG from monolayer as well as from bilayer graphene, where only AA and AB stacking are considered. Furthermore, the role of interband and intraband contributions are investigated in both the case. The role of interlayer coupling in HHG from bilayer graphene is investigated. Furthermore, polarisation and ellipticity dependences of the HHG are discussed. This paper is organised as follows: The theoretical model and numerical methods are presented in Sec. II. Sec. III presents the results and discussion of our numerical simulations, and the conclusions are presented in Sec. IV.

## II. NUMERICAL METHODS

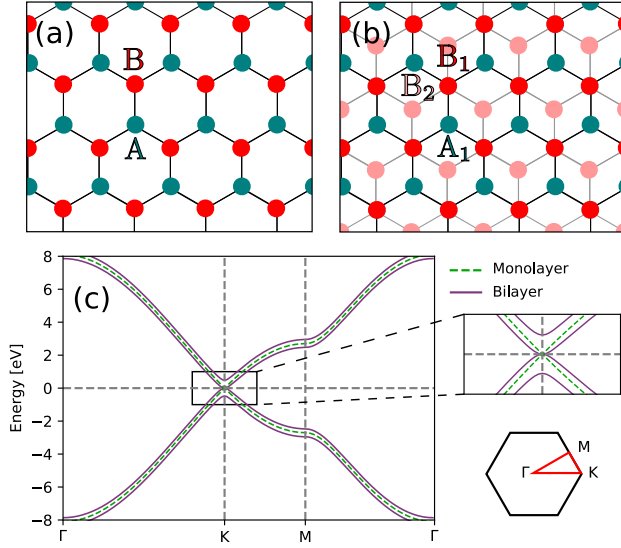


FIG. 1: The ground state of monolayer and bilayer graphene (AB-stacked). (a) and (b) show the top-view of the monolayer and bilayer graphene, respectively. The carbon atoms are arranged in a honeycomb lattice with two inequivalent carbon atoms (A and B). In bilayer graphene, the B atoms of the top layer are placed on top of A atoms of the bottom layer. (c) shows the band-structure of the monolayer (green) and bilayer graphene (violet).

The real-space lattice of monolayer graphene is shown in Fig. 1a. Carbon atoms are arranged in a honeycomb lattice with two-atom basis unit-cell. The A and B atoms in Fig. 1(a) represents two inequivalent carbon atoms in the unit-cell. The lattice parameter of graphene is equal

to 2.46 Å. Nearest-neighbour tight-binding approximation is implemented by only considering the  $p_z$  orbitals of the carbon atoms. The Hamiltonian for monolayer graphene is defined as

$$\hat{H}_0 = -t_0 f(\mathbf{k}) \hat{a}_k^\dagger \hat{b}_k + c.c. \quad (1)$$

Here,  $\hat{a}_k, \hat{b}_k$  are, respectively, the annihilation operators associated with A and B types of the atoms in the unit-cell.  $f(\mathbf{k})$  is defined as  $f(\mathbf{k}) = \sum_i e^{i\mathbf{k}\cdot\delta_i}$ , where  $\delta_i$  is the nearest neighbour vectors. A nearest-neighbour in-plane hopping energy  $t_0$  of 2.7 eV<sup>43</sup> is used. The eigenvalues of the Hamiltonian are given by  $\mathcal{E}(\mathbf{k}) = \pm t_0 |f(\mathbf{k})|$ .

Similarly, the Hamiltonian for AB-stacked bilayer graphene can be defined as

$$\hat{H}_{AB} = -t_0 f(\mathbf{k}) \left[ \hat{a}_{1k}^\dagger \hat{b}_{1k} + \hat{a}_{2k}^\dagger \hat{b}_{2k} \right] + t_\perp \hat{a}_{2k}^\dagger \hat{b}_{1k} + c.c. \quad (2)$$

Here, 1 and 2 denotes the atoms in the upper and lower layer, respectively. An inter-plane hopping energy,  $t_\perp$  of 0.48 eV is used for an inter-layer separation equal to 3.35 Å. The band-structure for the bilayer graphene is given by,  $\mathcal{E}(\mathbf{k}) = [\pm t_\perp \pm \sqrt{4f(\mathbf{k})^2 t_0^2 + t_\perp^2}]/2$ .

Figure 1(c) presents the energy band-structure of both monolayer and bilayer graphene. The band-structure of monolayer graphene has zero band-gap and linear dispersion near two points in the Brillouin zone (BZ), known as  $\mathbf{K}$ -points. On the other hand, bilayer graphene near  $\mathbf{K}$ -points shows a quadratic dispersion. Due to the zero band-gap nature, both monolayer and bilayer graphene are semi-metals in nature. Here, electron-hole symmetry is considered by neglecting higher-order hopping and overlap of the orbitals.

Semiconductor Bloch equations in Houston basis is solved as<sup>44-46</sup>

$$i \frac{d}{dt} \rho_{mn}^{\mathbf{k}} = \mathcal{E}_{mn}^{\mathbf{k}+\mathbf{A}(t)} \rho_{mn}^{\mathbf{k}} + i \frac{\tilde{\delta}_{mn}}{T_2} \rho_{mn}^{\mathbf{k}} - \mathbf{F}(t) \cdot \sum_l \left( \mathbf{d}_{ml}^{\mathbf{k}+\mathbf{A}(t)} \rho_{ln}^{\mathbf{k}} - \mathbf{d}_{ln}^{\mathbf{k}+\mathbf{A}(t)} \rho_{ml}^{\mathbf{k}} \right), \quad (3)$$

where  $\mathbf{F}(t)$  and  $\mathbf{A}(t)$  are the electric field and vector potential of the driving laser field, respectively; and are related as  $\mathbf{F}(t) = -d\mathbf{A}(t)/dt$ .  $\mathcal{E}_{mn}^{\mathbf{k}}$  and  $\mathbf{d}_{mn}^{\mathbf{k}}$  are the band-gap energy and the dipole-matrix elements between  $m$  and  $n$  bands, respectively. Here,  $\tilde{\delta}_{mn}$  is defined as  $(1 - \delta_{mn})$ .  $\mathbf{d}_{mn}$  are calculated as  $\mathbf{d}_{mn} = -i \langle u_{m,\mathbf{k}} | \nabla_{\mathbf{k}} | u_{n,\mathbf{k}} \rangle$ , where  $|u_{m,\mathbf{k}}\rangle$  is the periodic part of the wavefunction. A phenomenological term accounting for the decoherence is added, with a constant dephasing time  $T_2$  of 10 fs.

The total current at any  $\mathbf{k}$ -point in the BZ is calculated

as

$$\begin{aligned} \mathbf{J}(\mathbf{k}, t) &= \sum_{m,n} \rho_{mn}^{\mathbf{k}}(t) \mathbf{p}_{nm}^{\mathbf{k}+\mathbf{A}(t)} \\ &= \sum_{m \neq n} \rho_{mn}^{\mathbf{k}}(t) \mathbf{p}_{nm}^{\mathbf{k}+\mathbf{A}(t)} + \sum_{m=n} \rho_{mn}^{\mathbf{k}}(t) \mathbf{p}_{nm}^{\mathbf{k}+\mathbf{A}(t)} \\ &= \mathbf{J}_{inter}(\mathbf{k}, t) + \mathbf{J}_{intra}(\mathbf{k}, t). \end{aligned} \quad (4)$$

Here,  $\mathbf{J}_{inter}(\mathbf{k}, t)$  and  $\mathbf{J}_{intra}(\mathbf{k}, t)$  are interband and intraband contributions to the total current, respectively. The high-order harmonic spectrum is determined from

the Fourier-transform of the time-derivative of the current as

$$\mathcal{I}(\omega) = \left| \mathcal{FT} \left( \frac{d}{dt} \left[ \int_{BZ} \mathbf{J}(\mathbf{k}, t) d\mathbf{k} \right] \right) \right|^2. \quad (5)$$

In the present work, driving laser pulse with an intensity of  $1 \times 10^{11}$  W/cm<sup>2</sup> and wavelength of 3.2  $\mu\text{m}$  is used. The laser pulse is eight-cycles duration with a  $\sin^2$  envelope. The intensity of the driving pulse is much below the damage threshold and lower than the one used in experimental HHG from graphene<sup>23,25</sup>. The same parameters of the driving laser pulse are used throughout unless stated otherwise.

### III. RESULTS AND DISCUSSIONS

Figure 2 presents the HHG spectra of monolayer graphene and its comparison with the spectra of the bilayer graphene. Here, AB stacking of bilayer graphene is considered. The intensity of the HHG spectra is normalised with respect to the total number of electrons in monolayer and bilayer graphene. It is apparent that the third harmonic (H3) is matching well in both cases. However, harmonics higher than H3 show significantly different behaviour as the interlayer coupling between the two layers plays a role here.

The contributions of interband and intraband to the total harmonic spectra for monolayer and bilayer graphene are shown in Figs. 2(b) and (c), respectively. Both the contributions play a strong role to the total spectra as reflected from the figure. A strong interplay of interband and intraband contributions was reported for monolayer graphene<sup>22,25,26</sup>. Unlike the wide band-gap semiconductors, due to the vanishing band-gap, the interband and intraband transitions take place at the same energy scales for both monolayer and bilayer graphene<sup>47</sup>. The relative harmonic yield (integrated) from interband and intraband contributions are plotted in the insets of Figs. 2(b) and (c). Here, intraband contribution dominates upto third harmonics whereas interband contribution dominates for fifth (H5) and higher order harmonics for both monolayer and bilayer graphene. The increased contribution from interband transitions at higher orders can be attributed to the increased joint density of states at higher energies.

Also, as the low energy band-structure are different for monolayer and bilayer graphene [Fig. 1(c)], the nature of harmonic spectra is not obvious from the band-structure point of view. To have a better understanding of the underlying mechanism of harmonic generation in both cases, the role of interlayer coupling in HHG is discussed in the next subsection.

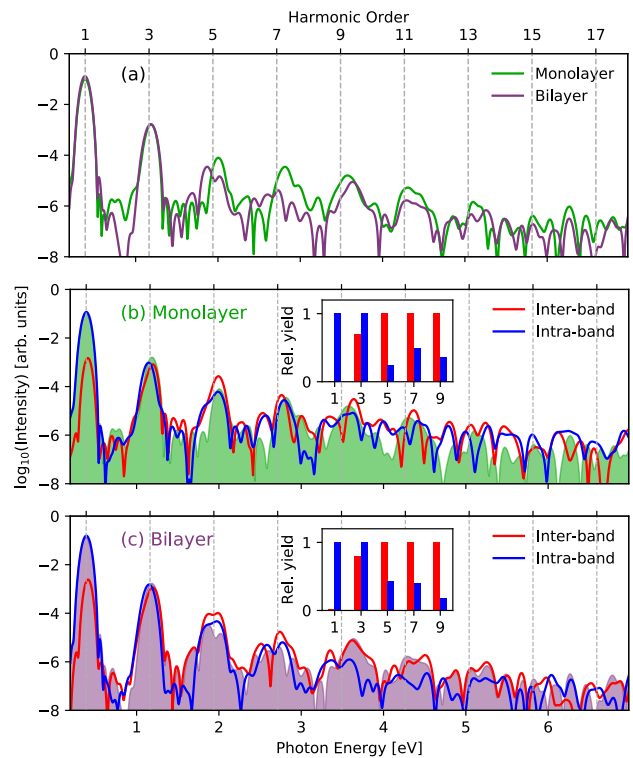


FIG. 2: (a) High-harmonic spectrum of the monolayer (green) and bilayer (violet) graphene with AB stacking. The high-harmonic intensity is normalised to the total number of electrons in monolayer and bilayer graphene. The interband and intraband contributions to the high-harmonic spectrum for (b) monolayer and (c) bilayer graphene. The total harmonic spectrum is also plotted for the reference. The relative harmonic yield (integrated) for different orders from interband and intraband contributions is plotted in the insets of (b) and (c), respectively.

#### A. Role of interlayer coupling in High-Harmonic Generation

To understand how the interlayer coupling between two layers affects the harmonic spectrum of bilayer graphene, the harmonic spectrum as a function of interlayer coupling strength ( $t_{\perp}$ ) is shown in Fig. 3(a). Reducing the interlayer coupling strength is equivalent of moving the two layers of graphene, in bilayer graphene, farther apart. The red dashed line in Fig. 3(a) corresponds to the interlayer coupling used in simulations shown in Fig. 2. It is evident from Fig. 3(a) that how H5 and higher-order harmonics are changing with respect to  $t_{\perp}$ . Moreover, different harmonic orders are affected differently. Therefore, all harmonic orders are non-linear functions of interlayer coupling.

To explore further how different hopping terms affect the HHG in bilayer graphene, an additional hopping term,  $t_3$ , between B atoms of the top layer and A atoms of the bottom layer is introduced. A hopping energy  $t_3$

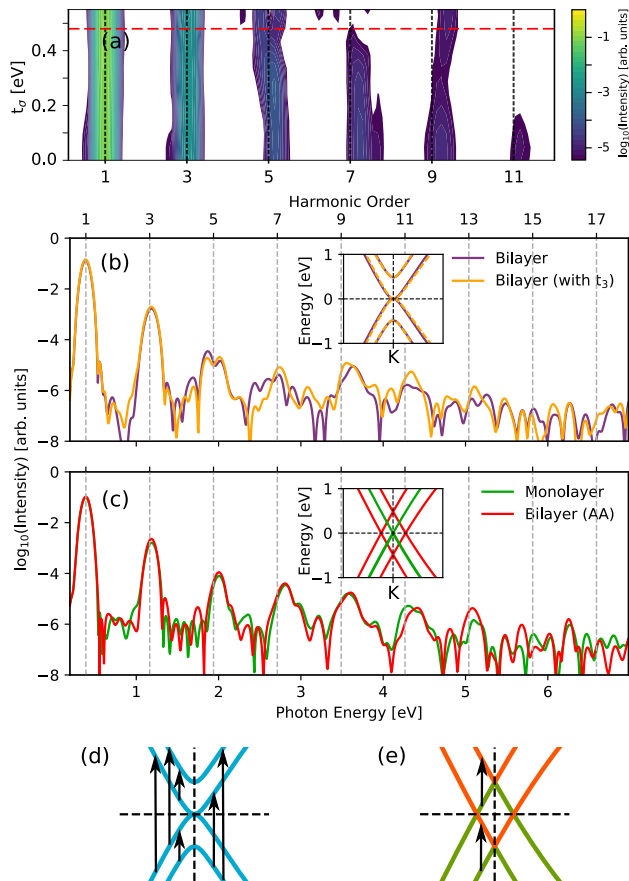


FIG. 3: (a) HHG spectrum of bilayer graphene with AB stacking as a function of interlayer coupling ( $t_{\perp}$ ), where  $t_{\perp} = 0$  corresponds to the HHG from monolayer graphene. The red dashed line corresponds to the actual value of  $t_{\perp}$  used in the calculations. (b) HHG from bilayer graphene (in AB stacking) with  $t_{\perp}$  ( $B_1$ - $A_2$ ) coupling only (violet) and with both  $t_{\perp}$  and  $t_3$  ( $A_1$ - $B_2$ ) coupling (orange). (c) HHG from bilayer graphene with AA stacking (red) and monolayer graphene (green). In (b) and (c) the band-structures near K-point are shown in the inset. (d) and (e) show the non-zero momentum matrix elements in AB and AA stacked bilayer graphene.

of 0.3 eV is used. The corresponding harmonic spectrum is presented in Fig. 3(b). It is evident from the figure that the additional interlayer coupling  $t_3$  affects all the harmonics higher than H3. This is apparent that the interlayer coupling has a strong role in determining the non-linear response of bilayer graphene.

Now let us discuss how HHG depends on different stacking configurations of the bilayer graphene. As discussed in the introduction, bilayer graphene can be realised in AA and AB stacking. AA stacking of bilayer graphene is realised by stacking the monolayer precisely on the top of the first layer. The top view of the AA-stacked bilayer looks exactly as monolayer graphene [Fig. 1(a)], where  $A_1$  couples with  $A_2$  and  $B_1$  couples with  $B_2$  with a coupling strength of  $t_{\perp}$ . The HHG spectra of

the bilayer graphene with AA configuration matches well with the spectrum of monolayer graphene as presented in Fig. 3(c).

The band-structures near  $\mathbf{K}$ -point are shown in the insets of Figs. 3(b) and (c). For AB-stacked bilayer graphene, a slight change in band-structure results in a significant change in the spectrum [see Fig. 3(b)]. On the other hand, for AA-stacked bilayer graphene, the difference in the band-structure is not reflected in the spectrum [see Fig. 3(c)].

A better understanding of the mechanism can be deduced by considering the roles of the band-structure as well as the interband momentum-matrix elements. The energy-bands of AA-stacked bilayer graphene within nearest neighbour tight-binding approximation are given by  $\mathcal{E}(\mathbf{k}) = \pm t_{\perp} \pm t_0 |f(\mathbf{k})|$ . This is equivalent of shifted energy-bands of monolayer graphene by  $\pm t_{\perp}$ . Also the corresponding momentum matrix elements give non-zero values only for the pairs  $t_{\perp} \pm t_0 |f(\mathbf{k})|$  and  $-t_{\perp} \pm t_0 |f(\mathbf{k})|$  as shown in Fig. 3(e). On the other hand, in AB-stacked bilayer graphene, all pairs of bands have non zero momentum matrix elements near  $\mathbf{K}$ -point as shown in Fig. 3(d). The similar band-dispersion and joint density-of-states compared to monolayer graphene results in similar harmonic spectrum in AA-stacked bilayer graphene. On the other hand, in bilayer graphene, an electron in the conduction band can recombine any of the valence bands near the  $\mathbf{K}$ -points as shown in Fig 3(d). These different interband channels interfere, generating the resulting harmonic spectrum of AB-stacked bilayer graphene.

From here onwards only bilayer graphene with AB stacking is considered as the HHG spectra of monolayer and bilayer graphene with AA stacking are same. In the next subsections, we explore polarisation and ellipticity dependences of the HHG from monolayer and bilayer graphene.

## B. Polarisation Dependence of the High-Harmonic Spectrum

The vector potential corresponds to a linearly polarised laser pulse can be defined as

$$\mathbf{A}(t) = A_0 f(t) \cos(\omega t) [\cos(\theta) \hat{\mathbf{e}}_x + \sin(\theta) \hat{\mathbf{e}}_y]. \quad (6)$$

Here,  $f(t)$  is the envelope function and  $\theta$  is the angle between laser polarisation and  $x$ -axis ( $\Gamma$ -K in the Brillouin zone).

The polarization-direction dependence of the harmonic yield for monolayer and bilayer graphene are presented in Figs. 4(a) and (b), respectively. All the harmonics mimic the six-fold symmetry of the graphene lattice. As reflected from the figure, H3 exhibits no significant polarization sensitivity for both monolayer and bilayer graphene. The reason for this isotropic nature can be attributed to the isotropic nature of energy-bands near  $\mathbf{K}$ -points. However, harmonics, higher than H3, show anisotropic behaviour in both cases. Moreover, H5 of

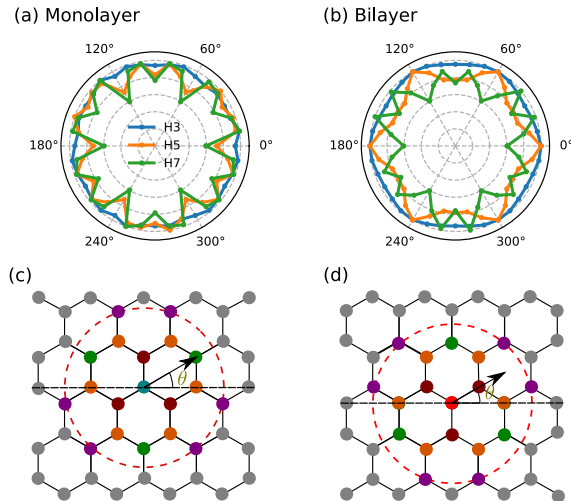


FIG. 4: Polarisation dependence of the normalised harmonic yield for (a) monolayer and (b) bilayer graphene. Here,  $\theta$  is an angle between laser polarisation and  $x$ -axis along  $-\mathbf{K}$  in the Brillouin zone. An illustration of the semi-classical real-space model with nearest neighbours of (a) A type and (d) B type carbon atoms. The first, second, third and fourth nearest neighbours are shown using brown, orange, green and violet colours, respectively.

monolayer and bilayer graphene shows different polarization dependence. The harmonic yield is maximum for angles close to  $15^\circ$  and  $45^\circ$  in monolayer graphene.

To understand the polarization dependence of the harmonic yield in monolayer graphene, we use a semiclassical explanation as proposed in Refs.<sup>48,49</sup>, by assuming the interband transitions can be translated to a semi-classical real-space model<sup>1,50</sup>. Such a one-to-one correspondence between interband transitions and inter-atom hopping in graphene was shown by Stroucken *et al.*<sup>47</sup>. Here, we assume that an electron can hop between two atoms when the laser is polarised along a direction in which it connects the atoms. The contributions to the harmonic yield from different pairs of atoms drop exponentially as the distance between the atoms increases. This is in principle governed by the inter-atom momentum matrix elements<sup>47</sup>. By assuming a finite radius for atoms, farther atoms show sharper intensity peaks as a function of angle of polarisation.

Figures 4(c) and (d) show the nearest neighbours of A and B type of atoms in the unit-cell, respectively. Brown, orange, green and violet coloured atoms are respectively first, second, third and fourth neighbours. By considering the nearest-neighbour hopping only in graphene, we can see that the maximum yield should be for  $30^\circ$  ( $\Gamma$ -M direction). However, the maximum yield is near  $15^\circ$  and  $45^\circ$  as seen from Fig. 4(a). This means that the contributions up to the fourth nearest neighbours should be considered to explain the polarisation dependence of H5 and seventh harmonic (H7) of monolayer graphene.

In bilayer graphene, H7 follows the same qualitative behaviour as that of H5 and H7 of monolayer graphene [Fig. 4(b)]. In contrast, H5 shows different behaviour and obeys the symmetry of the second nearest neighbour. It is clear from Fig. 3(d) that there are multiple paths for interband transitions for bilayer graphene. In bilayer graphene, interband transitions from different pairs of valence and conduction bands can contribute to a particular harmonic, and these different transitions interfere. This makes the mechanism of harmonic generation from monolayer and AB-stacked bilayer graphene different.

### C. Ellipticity Dependence of the High-Harmonic Spectrum

The ellipticity dependence of the monolayer (top panel) and bilayer graphene (bottom panel) are plotted in Fig. 5. The vector potential corresponds to the elliptically polarised pulse with an ellipticity  $\epsilon$  is defined as

$$\mathbf{A}(t) = \frac{A_0 f(t)}{\sqrt{1 + \epsilon^2}} [\cos(\omega t) \hat{\mathbf{e}}_x + \epsilon \sin(\omega t) \hat{\mathbf{e}}_y]. \quad (7)$$

Here, the same laser parameters mentioned in the Section II are used. The harmonic yield is normalised with respect to the harmonic yield for  $\epsilon = 0$ . The ellipticity dependence of all the three harmonics agrees qualitatively well for monolayer and bilayer graphene. The atomic-like ellipticity dependence of H3 can be attributed to its isotropic nature [see Figs. 5(a) and (b)]. However, H5 and H7 show a characteristic ellipticity dependence. The harmonic yield has a maximum for a finite value of the ellipticity and is polarised along the normal direction of the major axis of the ellipse. This interesting feature was observed for the monolayer graphene experimentally and explained as a consequence of the semi-metallic nature of the monolayer graphene<sup>23</sup>. Since bilayer graphene is also semi-metallic, it is also expected to exhibit similar ellipticity dependence, which we confirm here.

The different qualitative behaviour of the ellipticity dependence of H3 compared to H5 and H7 is also consistent with the finding that the interband and intraband mechanisms respond differently to the ellipticity of the laser<sup>51</sup> [See also insets of Figs. 2(b) and (c)]. The characteristic ellipticity dependence of monolayer graphene was shown to be dominating by interband contributions in Ref.<sup>26</sup>. The ellipticity of the maximum yield is different for bilayer graphene as a consequence of interlayer coupling.

## IV. CONCLUSIONS

In summary, HHG from monolayer and bilayer graphene having AA and AB stacking are discussed. The harmonic spectra of the monolayer and bilayer graphene are significantly different and exhibit characteristic features of having a vanishing band-gap. The HHG spec-

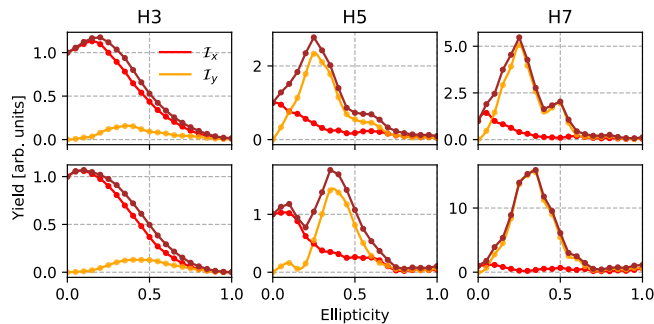


FIG. 5: Ellipticity dependence of the integrated harmonic yield for 3<sup>rd</sup> (H3), 5<sup>th</sup> (H5), and 7<sup>th</sup> (H7) harmonics of the monolayer (top panel) and bilayer graphene (bottom panel). The integrated harmonic yield, and its  $x$  and  $y$ -components are shown by black, red and orange colour lines, respectively. An elliptically polarised pulse with an intensity of  $1 \times 10^{11}$  W/cm<sup>2</sup> is used for HHG.

trum of the bilayer graphene shows signatures of the interlayer coupling, which affects high-order harmonics non-linearly and different harmonics are affected differently. This results in similar harmonic spectrum for monolayer and bilayer graphene with AA stacking. A strong interplay of interband and intraband contributions to the harmonic spectrum as well as their characteristic polarisation and ellipticity dependence is noticed in monolayer and bilayer graphene.

## V. ACKNOWLEDGMENTS

G. D. acknowledges support from Science and Engineering Research Board (SERB) India (Project No. ECR/2017/001460).

- 
- \* gdixit@phy.iitb.ac.in
- <sup>1</sup> S. Y. Kruchinin, F. Krausz, and V. S. Yakovlev, *Reviews of Modern Physics* **90**, 021002 (2018).
  - <sup>2</sup> S. Ghimire, A. D. DiChiara, E. Sistrunk, P. Agostini, L. F. DiMauro, and D. A. Reis, *Nature Physics* **7**, 138 (2011).
  - <sup>3</sup> S. Ghimire and D. A. Reis, *Nature Physics* **15**, 10 (2019).
  - <sup>4</sup> G. Vampa, T. J. Hammond, N. Thire, B. E. Schmidt, F. Legare, C. R. McDonald, T. Brabec, D. D. Klug, and P. B. Corkum, *Physical Review Letters* **115**, 193603 (2015).
  - <sup>5</sup> A. A. Lanin, E. A. Stepanov, A. B. Fedotov, and A. M. Zheltikov, *Optica* **4**, 516 (2017).
  - <sup>6</sup> N. Tancogne-Dejean, O. D. Mucke, F. X. Kartner, and A. Rubio, *Physical Review Letters* **118**, 087403 (2017).
  - <sup>7</sup> M. S. Mrudul, N. Tancogne-Dejean, A. Rubio, and G. Dixit, *npj Computational Materials* **6**, 1 (2020).
  - <sup>8</sup> A. Pattanayak, M. S. Mrudul, and G. Dixit, *Physical Review A* **101**, 013404 (2020).
  - <sup>9</sup> T. T. Luu, M. Garg, S. Y. Kruchinin, A. Moulet, M. T. Hassan, and E. Goulielmakis, *Nature* **521**, 498 (2015).
  - <sup>10</sup> M. Garg, M. Zhan, T. T. Luu, H. Lakhota, T. Klostermann, A. Guggenmos, and E. Goulielmakis, *Nature* **538**, 359 (2016).
  - <sup>11</sup> O. Schubert, M. Hohenleutner, F. Langer, B. Urbanek, C. Lange, U. Huttner, D. Golde, T. Meier, M. Kira, S. W. Koch, et al., *Nature Photonics* **8**, 119 (2014).
  - <sup>12</sup> C. R. McDonald, G. Vampa, P. B. Corkum, and T. Brabec, *Physical Review A* **92**, 033845 (2015).
  - <sup>13</sup> Z. Nourbakhsh, N. Tancogne-Dejean, H. Merdji, and A. Rubio, *arXiv preprint arXiv:2010.08010* (2020).
  - <sup>14</sup> A. K. Geim, *Science* **324**, 1530 (2009).
  - <sup>15</sup> K. S. Novoselov, A. K. Geim, S. V. Morozov, D. Jiang, Y. Zhang, S. V. Dubonos, I. V. Grigorieva, and A. A. Firsov, *Science* **306**, 666 (2004).
  - <sup>16</sup> H. K. Avetissian and G. F. Mkrtchian, *Physical Review B* **94**, 045419 (2016).
  - <sup>17</sup> E. Hendry, P. J. Hale, J. Moger, A. K. Savchenko, and S. A. Mikhailov, *Physical Review Letters* **105**, 097401 (2010).
  - <sup>18</sup> N. Kumar, J. Kumar, C. Gerstenkorn, R. Wang, H. Y. Chiu, A. L. Smirl, and H. Zhao, *Physical Review B* **87**, 121406 (2013).
  - <sup>19</sup> H. A. Hafez, S. Kovalev, J.-C. Deinert, Z. Mics, B. Green, N. Awari, M. Chen, S. Germanskiy, U. Lehnert, J. Teichert, et al., *Nature* **561**, 507 (2018).
  - <sup>20</sup> H. Avetissian and G. Mkrtchian, *Physical Review B* **97**, 115454 (2018).
  - <sup>21</sup> L. A. Chizhova, F. Libisch, and J. Burgdorfer, *Physical Review B* **95**, 085436 (2017).
  - <sup>22</sup> I. Al-Naib, J. Sipe, and M. M. Dignam, *Physical Review B* **90**, 245423 (2014).
  - <sup>23</sup> N. Yoshikawa, T. Tamaya, and K. Tanaka, *Science* **356**, 736 (2017).
  - <sup>24</sup> O. Zurrón-Cifuentes, R. Boyero-García, C. Hernández-García, A. Picon, and L. Plaja, *Optics express* **27**, 7776 (2019).
  - <sup>25</sup> M. Taucer, T. Hammond, P. Corkum, G. Vampa, C. Couture, N. Thire, B. Schmidt, F. Legare, H. Selvi, N. Unsure, et al., *Physical Review B* **96**, 195420 (2017).
  - <sup>26</sup> C. Liu, Y. Zheng, Z. Zeng, and R. Li, *Physical Review A* **97**, 063412 (2018).
  - <sup>27</sup> Z.-Y. Chen and R. Qin, *Optics express* **27**, 3761 (2019).
  - <sup>28</sup> S. A. Mikhailov, *EPL (Europhysics Letters)* **79**, 27002 (2007).
  - <sup>29</sup> A. K. Gupta, O. E. Alon, and N. Moiseyev, *Physical Review B* **68**, 205101 (2003).
  - <sup>30</sup> M. S. Mrudul, A. Jimenez-Galan, M. Ivanov, and G. Dixit, *arXiv preprint arXiv:2011.04973* (2020).
  - <sup>31</sup> O. Zurrón, A. Picon, and L. Plaja, *New Journal of Physics* **20**, 053033 (2018).
  - <sup>32</sup> G. Vampa, C. R. McDonald, G. Orlando, D. D. Klug, P. B. Corkum, and T. Brabec, *Physical Review Letters* **113**, 073901 (2014).
  - <sup>33</sup> H. K. Kelardeh, V. Apalkov, and M. I. Stockman, *Physical Review B* **91**, 045439 (2015).
  - <sup>34</sup> T. Tamaya, A. Ishikawa, T. Ogawa, and K. Tanaka, *Physical review letters* **116**, 016601 (2016).
  - <sup>35</sup> H. Yan, X. Li, B. Chandra, G. Tulevski, Y. Wu, M. Freitag, W. Zhu, P. Avouris, and F. Xia, *Nature Nanotechnology*

- 7, 330 (2012).
- <sup>36</sup> A. V. Rozhkov, A. O. Sboyshakov, A. L. Rakhmanov, and F. Nori, *Physics Reports* **648**, 1 (2016).
- <sup>37</sup> E. McCann and M. Koshino, *Reports on Progress in Physics* **76**, 056503 (2013).
- <sup>38</sup> S. Ulstrup, J. C. Johannsen, F. Cilento, J. A. Miwa, A. Crepaldi, M. Zacchigna, C. Cacho, R. Chapman, E. Springate, S. Mammadov, et al., *Physical review letters* **112**, 257401 (2014).
- <sup>39</sup> P. Kumar, T. M. Herath, V. Apalkov, and M. I. Stockman, *arXiv preprint arXiv:2004.09732* (2020).
- <sup>40</sup> P. Kumar, T. M. Herath, V. Apalkov, and M. I. Stockman, *arXiv preprint arXiv:2007.13480* (2020).
- <sup>41</sup> H. Avetissian, G. Mkrtchian, K. Batrakov, S. Maksimenko, and A. Ho mann, *Physical Review B* **88**, 165411 (2013).
- <sup>42</sup> T. N. Ikeda, *Physical Review Research* **2**, 032015 (2020), URL <https://link.aps.org/doi/10.1103/PhysRevResearch.2.032015>.
- <sup>43</sup> S. Reich, J. Maultzsch, C. Thomsen, and P. Ordejon, *Physical Review B* **66**, 035412 (2002).
- <sup>44</sup> W. Houston, *Physical Review* **57**, 184 (1940).
- <sup>45</sup> J. Krieger and G. Iafrate, *Physical Review B* **33**, 5494 (1986).
- <sup>46</sup> I. Floss, C. Lemell, G. Wachter, V. Smejkal, S. A. Sato, X.-M. Tong, K. Yabana, and J. Burgdorfer, *Physical Review A* **97**, 011401 (2018).
- <sup>47</sup> T. Stroucken, J. Gronqvist, and S. Koch, *Physical Review B* **84**, 205445 (2011).
- <sup>48</sup> Y. S. You, D. A. Reis, and S. Ghimire, *Nature physics* **13**, 345 (2017).
- <sup>49</sup> M. S. Mrudul, A. Pattanayak, M. Ivanov, and G. Dixit, *Physical Review A* **100**, 043420 (2019).
- <sup>50</sup> A. M. Parks, G. Ernotte, A. Thorpe, C. R. McDonald, P. B. Corkum, M. Taucer, and T. Brabec, *arXiv preprint arXiv:2006.09651* (2020).
- <sup>51</sup> N. Tancogne-Dejean, O. D. Mucke, F. X. Kartner, and A. Rubio, *Nature Communications* **8**, 745 (2017).